ADVANCED FUNCTIONAL MATERIALS
www.afm-journal.de

Protease-Activatable Nanozyme with Photoacoustic and Tumor-Enhanced Magnetic Resonance Imaging for Photothermal Ferroptosis Cancer Therapy

*Wen Qin, Jinzhao Huang, Chunsheng Yang, Quer Yue, Shizhen Chen, Mengdie Wang, Shangbang Gao, Xin Zhou, Xiangliang Yang, and Yan Zhang**

Despite the promise of ferrotherapy in cancer treatment, current ferrous therapeutics suffer from compromised antitumor ferroptosis efficacy and low specificity for tumors. Herein, a protease-activatable nanozyme (Fe_3O_4@$Cu_{1.77}Se$) is reported for photoacoustic and tumor-enhanced magnetic resonance imaging (MRI)-guided second near-IR photothermal ferroptosis cancer therapy. Fe_3O_4@$Cu_{1.77}Se$ remains stable in physiological conditions, but disintegrates to increase reactive intratumoral ferrous supply for elevated hydroxyl radical generation by Fenton reaction and GSH depletion in response to overexpressed matrix metalloproteinases in tumor microenvironment, leading to amplified ferroptosis of tumor cells as well as enhanced T_2-weighted MRI contrast. Further integration with second near-IR photoirradiation to generate localized heat not only triggers effective photothermal therapy and photoacoustic imaging but more importantly, potentiates Fenton reaction to promote ferroptotic tumor cell death. Such synergism leads to the polarization of tumor-associated macrophage from the tumor-promoting M2 type to the tumor-killing M1 type, and induces the immunogenic cells death of tumor cells, which in turn promotes the maturation of dendritic cells and infiltration of cytotoxic T lymphocytes in tumor, contributing to significant tumor suppression. This study presents a novel activatable ferrous nanotheranostics for spatial-temporal control over antitumor ferroptosis responses.

1. Introduction

Ferroptosis refers to a new non-apoptotic programmed cell death pathway that mainly relies on iron-dependent catalytic conversion of endogenous hydrogen peroxide (H_2O_2) into highly cytotoxic hydroxyl radical (•OH) to induce a lethal level of lipid peroxidation (LPO).[1] Distinct from apoptosis, necrosis, and autophagy, ferroptosis is not affected by the common tumor-associated mutations such as upregulation of anti-apoptotic proteins or downregulation of pro-apoptotic proteins and thus, offers a promising anti-tumor therapeutic strategy. Considering the vital role of iron in ferroptosis induction, a variety of small-molecule or iron-based nanotherapeutics, such as ferumoxytol,[2] amorphous iron nanoparticles,[3] inorganic iron nanoparticles,[4] and iron–organic frameworks,[5] has been developed. Unfortunately, the unfavorable tumor microenvironment (TME) compromises their catalytic activities, and thus, are often required a very high dosage of iron (75 mg kg^{-1} body weight by intravenous injection) to achieve desirable tumor inhibition.[6] The nonspecific biodistribution and "always-on" pharmacological activities of iron-based therapeutic agents would inevitably incur the "off-target" toxicity, which may cause collateral side effects toward normal tissues. To mitigate the damage to normal tissues and boost the therapeutic efficacy, current efforts have been devoted to designing stimuli-responsive nano-therapeutics, of which

W. Qin, J. Huang, S. Gao, X. Yang, Y. Zhang
National Research Centre for Nanomedicine
College of Life Science and Technology
Huazhong University of Science and Technology
Wuhan 430074, P. R. China
E-mail: yan_zhang@hust.edu.cn

C. Yang, Q. Yue, S. Chen, X. Zhou
State Key Laboratory of Magnetic Resonance and Atomic and Molecular Physics National Center for Magnetic Resonance in Wuhan
Wuhan Institute of Physics and Mathematics Innovation Academy of Precision Measurement Science and Technology
Chinese Academy of Sciences
Wuhan 430071, P. R. China

M. Wang
Department of Neurology
Union Hospital
Tongji Medical College
Huazhong University of Science and Technology
Jiefang Avenue, Wuhan 430022, P. R. China

X. Yang, Y. Zhang
Hubei Key Laboratory of Bioinorganic Chemistry and Materia Medical
Huazhong University of Science and Technology
Wuhan 430074, P. R. China

The ORCID identification number(s) for the author(s) of this article can be found under https://doi.org/10.1002/adfm.202209748.

DOI: 10.1002/adfm.202209748

the therapeutic abilities could be "turned on" in response to specific stimuli in tumor or within TME (e.g., low pH, highly expressed enzyme, hypoxia, etc.).[7] These nanoplatforms have shown tumor-specific therapeutic activation with reduced toxicity, which are however less investigated in tumor-specific ferrotherapy.

To enhance anti-tumor ferrotherapeutic performance, elevated temperature in the presence of photothermal conversion materials was reported to accelerate the Fenton reaction kinetics.[8] On the one hand, the photoirradiation facilities the reactive oxygen species (ROS) generation of iron-therapeutics through direct electron transfer and photo-enhanced Fenton reaction, and concurrently, the ROS generation can be improved by the photothermal effect.[9] Kinetics studies indicate that the Fenton reaction rate was enhanced by up to four folds upon increasing the temperature from 20 to 50 °C.[6] On the other hand, hyperthermia affects intracellular enzymatic activity and breaks the inherent resistance (e.g., ferroptosis-related proteins, labile iron pool, and respiratory enzymes) of cancer cells, and thus, generating desirable anti-tumor therapeutic effects. Compared to the conventional first near-IR (NIR-I, 700–1000 nm) window, second near-IR (NIR-II, 1000–1700 nm) window exhibits significantly reduced tissue attenuation, deep tissue penetration along with elevated maximum permissible energy exposure to skin of light,[10] and thus, has inspired researchers to constantly explore NIR-II photothermal materials including gold nanoparticles,[11] carbon materials,[12] copper sulfide-based nanoparticles,[13] and organic polymer[14] through precise particle size/morphology control, delicate surface modification or component selection. Considerable investigations were conducted for photothermal-enhanced Fenton nanoagents,[8a] which only a few examples were reported for in vivo NIR-II photothermal ferrotherapy, including transformable semiconducting nanozyme,[15] single-atom Pd nanozyme,[16] cysteine-responsive charge-transfer complex nanoparticles.[17] However, modulating the TME-activatable nanozyme in hybrid cancer NIR-II ferrotherapy has been underexploited so far. Moreover, the mechanistic investigation responsible for the effective inhibition of tumor and metastasis remains elusive.

Herein, we report a nanozyme (Fe_3O_4@$Cu_{1.77}Se$) with protease-activatable, NIR-II photothermal-enhanced catalytic and GSH depletion activities for photoacoustic (PA) and magnetic resonance imaging (MRI)-guided photothermal ferroptosis cancer therapy (**Scheme 1**). Gelatin, a polypeptide that can be degraded by matrix metalloproteinases (MMPs), such as MMP-2 or MMP-9, overexpressed in TME, serves as template

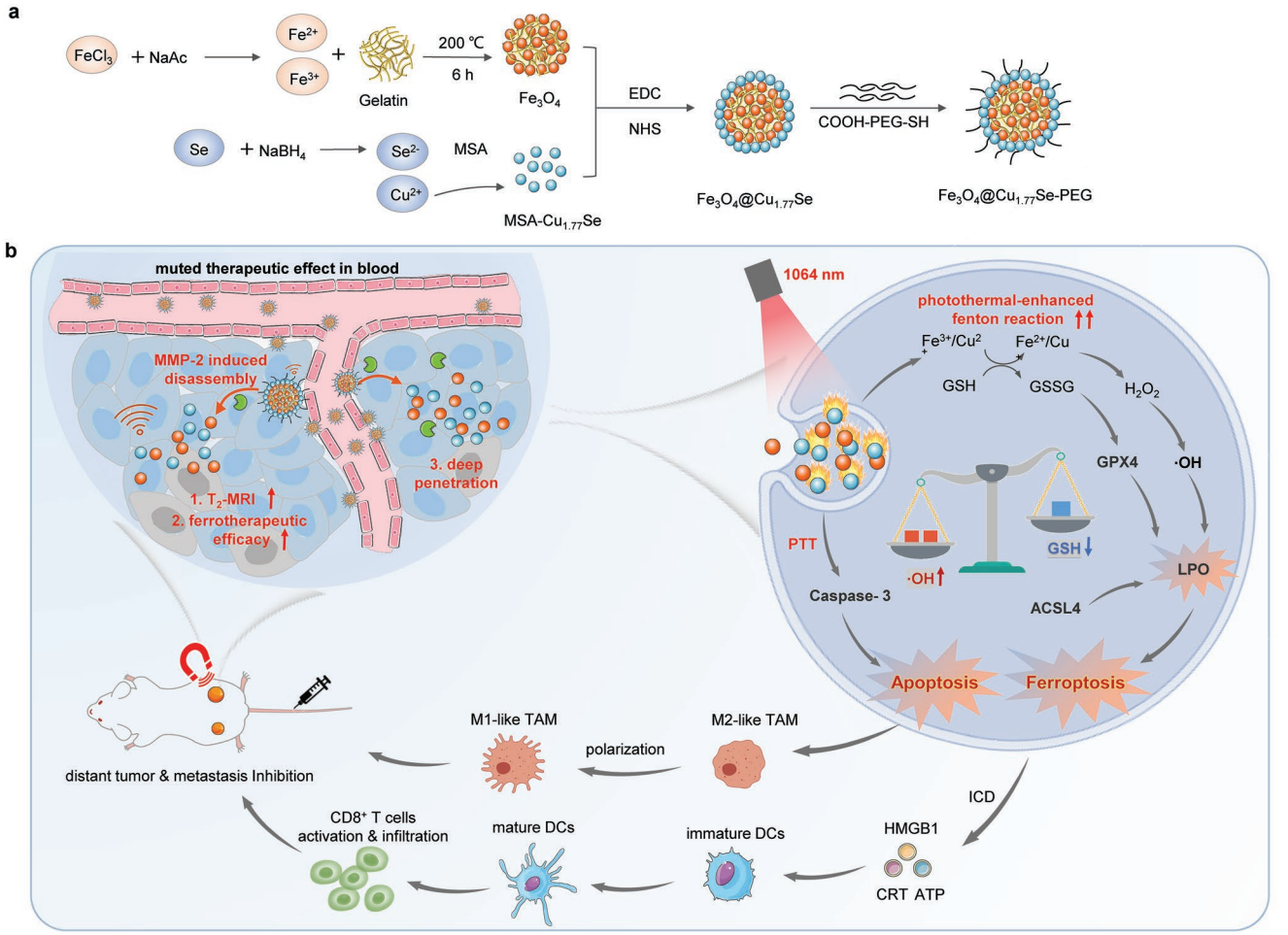

Scheme 1. a) Synthesis and b) biological mechanism of MMP-2-activatable Fe_3O_4@$Cu_{1.77}Se$ nanozymes with enhanced MR-imaging for second near-IR photothermal ferroptosis cancer therapy.

for the assembly of superparamagnetic Fe_3O_4 nanoparticles into Fe_3O_4 nanoclusters, followed by the conjugation of $Cu_{1.77}Se$ via EDC/NHS chemistry (Scheme 1a). The nanozymes remain intact followed by systematic circulation and their magnetic-responsive behavior allows the magnetic field-guided delivery to tumor site. Upon reaching the tumor site, the overexpressed MMPs in the TME disassemble the Fe_3O_4@$Cu_{1.77}Se$, not only transforming them from 124.2 nm into small fragments (≈14.6 ± 6.9 nm), favoring deep penetration into solid tumor, but also enhance intratumoral iron pool to elevate the T_2-weighted MRI contrast and the ferrotherapeutic effect (Scheme 1b). Further NIR-II photoirradiation to induce localized heat not only triggers effective PTT to enhance the apoptosis but also significantly potentiates Fenton reaction to generate hydroxyl radical and deplete GSH to induce more lipid peroxidation (LPO) for enhanced ferroptosis. Such synergism polarizes M2 tumor-associated macrophages to M1 tumor-associated macrophages, and also, induces immunogenic cell death to enhance the recruitment and infiltration of cytotoxic T cells into the immunogenetic cold tumor (4T1). Therefore, it not only leads to the elimination of primary tumor, but also elicits systemic anti-tumor immunity, contributing to regression of non-treated distant tumors and inhibition of lung metastasis. The combinational on-site and precise spatial-temporal activation strategy triggers the therapeutic process specifically within tumor tissues rather than normal ones, resulting in the concurrent high photothermal ferroptosis cancer therapeutic efficacy and negligible damage to normal tissues.

2. Results and Discussion

The nanozyme, Fe_3O_4@$Cu_{1.77}Se$, was prepared via a step-by-step conjugation. Briefly, Fe_3O_4 nanoclusters, assembled from superparamagnetic Fe_3O_4 nanoparticles with gelatin as a mediator, serve as seeds, followed by conjugation of $Cu_{1.77}Se$ via seed-mediated growth. Transmission electron microscopy (TEM) images showed that Fe_3O_4, $Cu_{1.77}Se$, and Fe_3O_4@$Cu_{1.77}Se$ were uniform, spherical and monodisperse, with the diameters determined to be 116.2 ± 7.1, 4.1 ± 1.3, and 124.2 ± 3.0 nm, respectively (**Figure 1**a; Figures S1, S2, Supporting Information). The lattice distance of 0.21 and 0.33 nm in the high-resolution TEM (HRTEM) images of Fe_3O_4@$Cu_{1.77}Se$ correlated with the (400) and (111) plane of Fe_3O_4 and $Cu_{1.77}Se$, respectively (Figure 1b). Elemental mappings revealed the presence and homogeneous distribution of Fe, O, Cu, and Se elements in the entire architecture of Fe_3O_4@$Cu_{1.77}Se$ (Figure 1c). X-ray photoelectron spectroscopy (XPS) further confirmed the presence of Cu, Fe, and Se in Fe_3O_4@$Cu_{1.77}Se$ (Figures 1d,e; Figure S3, Supporting Information). Mixed valences of Cu^{2+} (binding energy at 933.6 and 954.1 eV) and Cu^{+} (binding energy at 932.2 and 952.1 eV) were assigned to the peaks of Cu $2p_{3/2}$ and Cu $2p_{1/2}$, respectively. The content of Cu^{2+} and Cu^{+} was calculated to be 12.9% and 87.1%, respectively. The peaks centered at 709.6 and 719.3 eV in the Fe $2p_{3/2}$ spectrum can be assigned to Fe^{2+} and Fe^{3+}, respectively. The content of Fe^{2+} and Fe^{3+} in the nanozymes was determined to be 50.5% and 49.5%, respectively. Consistently, the molar ratio of Fe/Cu in the nanozymes, characterized by the inductively coupled plasma optical emission spectrometer (ICP-OES), was determined to be ≈1:0.83 (Table S1, Supporting Information). X-ray diffraction (XRD) patterns revealed the presence of Fe_3O_4 (JCPDS 19–0629) and $Cu_{2-x}Se$ (JCPDS 06–0680) peaks in Fe_3O_4@$Cu_{1.77}Se$ (Figure 1f). Magnetic hysteresis loops indicated that Fe_3O_4 and Fe_3O_4@$Cu_{1.77}Se$ were superparamagnetic at room temperature, with the saturation magnetization values of 71.9 and 44.6 emu g^{-1}, respectively (Figure 1g).

Next, the photothermal properties of Fe_3O_4@$Cu_{1.77}Se$ were investigated. Fe_3O_4 had very low NIR-II absorption, regardless of a broad absorption from visible to NIR region (Figure S4, Supporting Information). After conjugation with $Cu_{1.77}Se$, a significantly enhanced absorption peak from visible to NIR-II range, especially from 1000 to 1400 nm, was observed, indicating the potential of Fe_3O_4@$Cu_{1.77}Se$ as NIR-II photothermal agents. Therefore, upon 1064 nm photoirradiation, Fe_3O_4@$Cu_{1.77}Se$ exhibited power-dependent temperature increase (Figure 1h; Figure S5, Supporting Information). The maximum temperature reached ≈53 °C at Fe_3O_4@$Cu_{1.77}Se$ concentration of 100 μg mL^{-1} in 10 min (0.75 W cm^{-2}), whereas water showed negligible temperature increase (Figure S6, Supporting Information). The photothermal conversion efficacy (η) was determined to be 67.6% (Figure 1i). Moreover, Fe_3O_4@$Cu_{1.77}Se$ displayed excellent photostability after five heating and cooling cycles under NIR-II photoirradiation (Figure S7, Supporting Information). Noted that Fe_3O_4@$Cu_{1.77}Se$ remained in the original morphology and absorbance after photoirradiation, suggesting that Fe_3O_4@$Cu_{1.77}Se$ could not be collapsed into small nanoparticles with elevated temperature (Figures S8, S9, Supporting Information).

To enhance the in vivo stability and biocompatibility of Fe_3O_4@$Cu_{1.77}Se$, PEG was afterward conjugated on their surface. Dynamic light scattering (DLS) showed Fe_3O_4@$Cu_{1.77}Se$ -PEG had the hydrodynamic size of 195 nm and good colloidal stability up to 7 days in water (Figure S10, Supporting Information). Zeta potentials of Fe_3O_4, $Cu_{1.77}Se$, Fe_3O_4@$Cu_{1.77}Se$, and Fe_3O_4@$Cu_{1.77}Se$-PEG were 8, –17, –8.5, and –12 mV, respectively (Figure S11, Supporting Information). The strong band at 588 cm^{-1} of Fe_3O_4 in Fourier transform IR (FTIR) spectroscopy was due to Fe–O vibration, which was weakened and shifted to 581 cm^{-1} for Fe_3O_4@$Cu_{1.77}Se$. The peaks at 1053 (C—O groups), 1632 (characteristic C=C stretching groups), 2845 and 2924 cm^{-1} (asymmetric and symmetric stretching vibrations of $–CH_2–$ groups, respectively), and 3437 cm^{-1} (–OH groups), proving the existence of gelatin, were all weakened after $Cu_{1.77}Se$ conjugation (Figure S12, Supporting Information). Thermogravimetric analysis (TGA) further indicated the content of gelatin, MSA, and PEG in Fe_3O_4@$Cu_{1.77}Se$ was 6.52%, 12.74%, and 4.83%, respectively (Figure S13, Supporting Information).

Next, MMP-2 activatable, NIR-II photothermal-enhanced catalytic activities, and glutathione (GSH) depletion capabilities of Fe_3O_4@$Cu_{1.77}Se$ were examined. Fe_3O_4@$Cu_{1.77}Se$ was pretreated with or without MMP-2 for different time intervals, and generation of hydroxyl radicals (•OH) and depletion of GSH were then evaluated by monitoring the decreased absorption of methylene blue (MB) and 5,5'-dithiobis (2-nitrobenzoic acid) (DTNB), respectively (**Figure 2**a). MB can be degraded by •OH to form MB-OH with low absorbance ranging from 600 to 750 nm in UV–vis spectroscopy, while DTNB can be reduced by

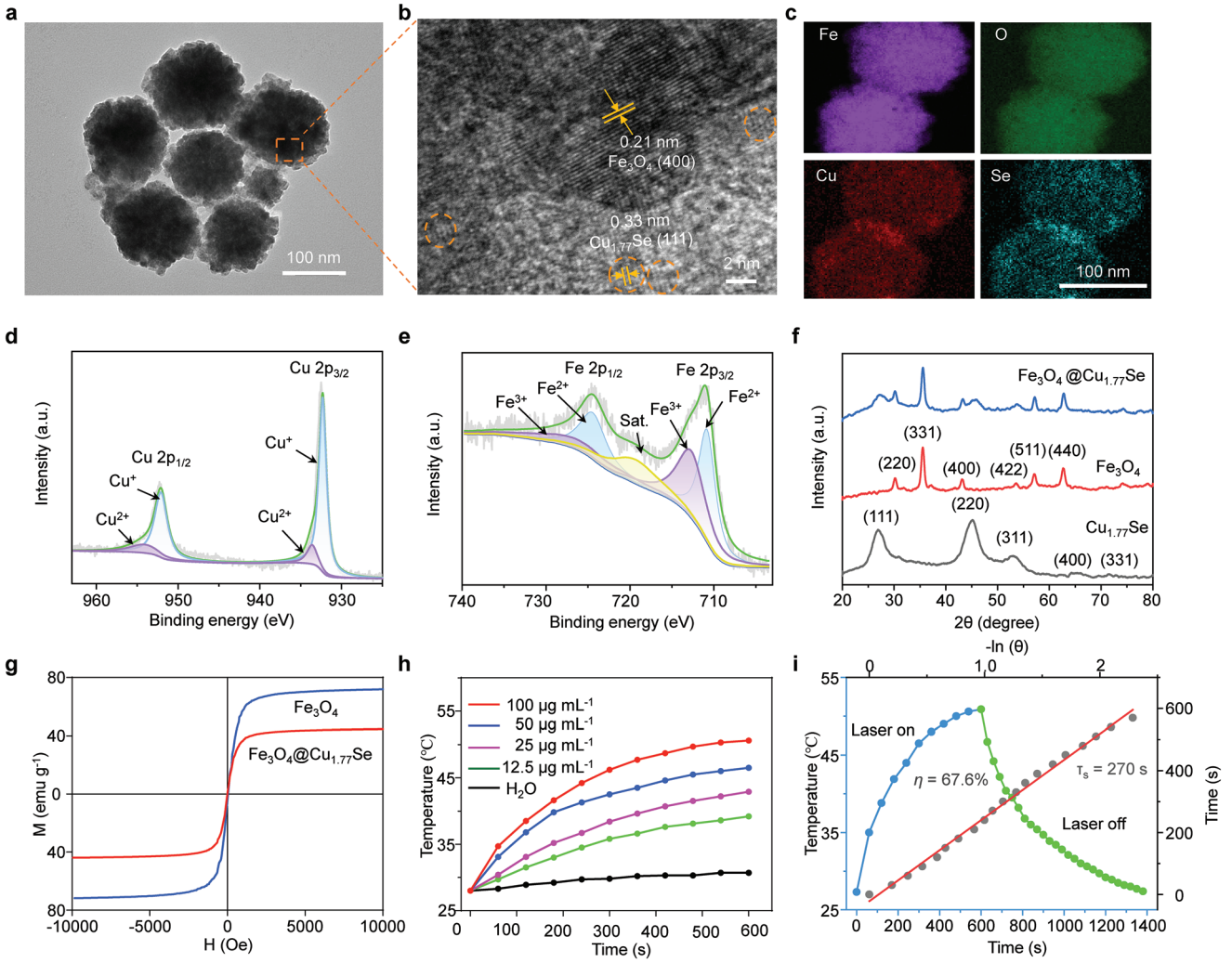

Figure 1. Synthesis and characterization of Fe_3O_4@$Cu_{1.77}Se$ nanozymes. a) TEM, b) HRTEM images, and c) elemental mapping of Fe_3O_4@$Cu_{1.77}Se$. XPS spectra of d) Cu and (e) Fe in Fe_3O_4@$Cu_{1.77}Se$. f) Powder XRD patterns of Fe_3O_4 (JCPDS 19-0629), $Cu_{1.77}Se$ (JCPDS 06-0680), and Fe_3O_4@$Cu_{1.77}Se$. g) Room temperature magnetization curve of Fe_3O_4 and Fe_3O_4@$Cu_{1.77}Se$. h) Photothermal curves of Fe_3O_4@$Cu_{1.77}Se$ with different concentrations and DI water upon second NIR photoirradiation (1064 nm, 0.75 W cm^{-2}). i) Photothermal profile of Fe_3O_4@$Cu_{1.77}Se$ (50 μg mL^{-1}) under second NIR photoirradiation (1064 nm, 0.75 W cm^{-2}) for 10 min, followed by natural cooling to room temperature, and linear time data versus ln(θ) acquired from the cooling period of panel.

GSH to form 2-nitro-5-thiobenzoic acid with maximal absorption at 412 nm. As shown in Figure 2b, in the presence of H_2O_2 (5 mM, mimicking the TME), the bleach of MB absorbance from Fe_3O_4@$Cu_{1.77}Se$ pretreated with MMP-2 for 48 h was the fastest, followed by 24 and 0 h at each tested time points, whereas it remained unchanged in non-MMP-2 treated groups. This indicated that the presence of MMP-2 accelerated the decomposition of H_2O_2 by Fe_3O_4@$Cu_{1.77}Se$ to generate •OH in a time-dependent manner. At 10 min, the MB absorbance (A_{10}/A_0) at 48 h was 1.3-, 1.9- and 1.9-fold lower than those at 24, 0 h, and non MMP-2 pretreated groups, respectively (Figure S14, Supporting Information). Subsequently, the catalytic activities of Fe_3O_4@$Cu_{1.77}Se$ were compared to those of Fe_3O_4 and $Cu_{1.77}Se$ with or without pretreatment of MMP-2 for 48 h, respectively (Figure 2c). Fe_3O_4@$Cu_{1.77}Se$ exhibited the fastest MB degradation capabilities, followed by $Cu_{1.77}Se$ and Fe_3O_4 at each test time point in non-MMP-2 pretreated groups. The higher catalytic activities of $Cu_{1.77}Se$ compared to Fe_3O_4 are due to higher Fenton-like reaction kinetics of Cu^+ ions compared to Fe^{2+} ions. The catalytic ability of Fe_3O_4@$Cu_{1.77}Se$ was further enhanced upon MMP-2 pretreatment. Specifically, at 10 min, MB bleach of Fe_3O_4@$Cu_{1.77}Se$ was 66.8%, 1.9-, 2.1-, and 1.7-fold lower than that in Fe_3O_4@$Cu_{1.77}Se$, Fe_3O_4+MMP-2, and $Cu_{1.77}Se$+MMP-2 groups, respectively. Notably, upon combinational 10 min photoirradiation, MB bleaching by Fe_3O_4@$Cu_{1.77}Se$ with MMP-2 pretreatment was decreased from 66.8% to 44.5%, confirming that NIR-II photothermal effect significantly accelerated the Fenton reaction rate.

The catalytic efficacy was then evaluated by incubating Fe_3O_4@$Cu_{1.77}Se$ with different concentrations of H_2O_2 in the presence of MMP-2 at 0 and 48 h, respectively. K_m of Fe_3O_4@$Cu_{1.77}Se$ incubated with MMP-2 for 0 and 48 h were determined to be 11.46 and 9.77 mM, respectively. Meanwhile, V_m of Fe_3O_4@$Cu_{1.77}Se$ incubated with MMP-2 for 0 and 48 h were 3.57×10^{-8} and

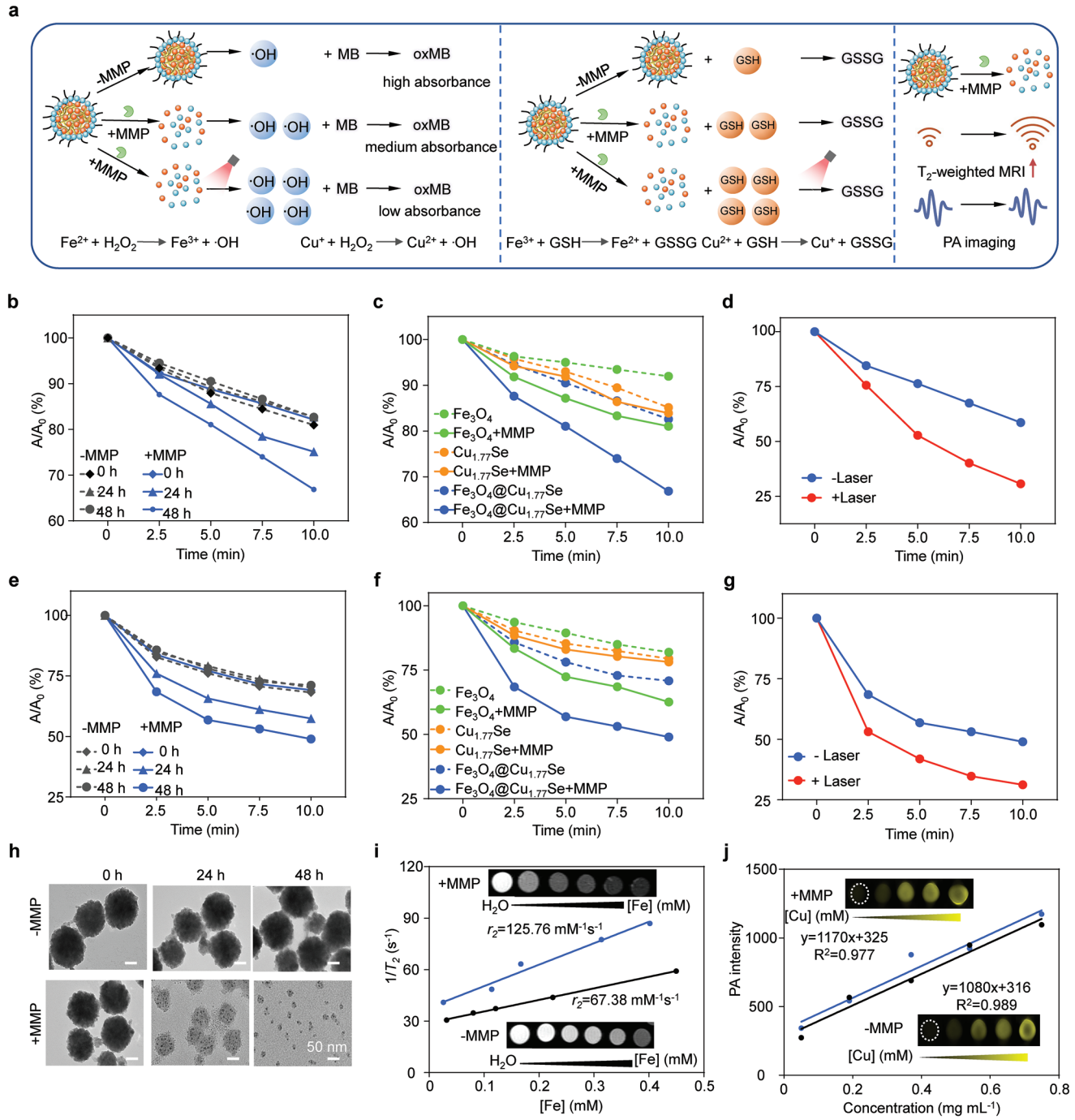

Figure 2. In vitro MMP-2 activatable, second-photothermal boosted catalytic behavior, GSH depletion, and imaging of Fe_3O_4@$Cu_{1.77}Se$ upon treatments. a) Diagram for MMP-2 activatable and NIR-II photoirradiation boosted •OH generation, GSH depletion, and MR/PA imaging of Fe_3O_4@$Cu_{1.77}Se$. b) MB degradation of Fe_3O_4@$Cu_{1.77}Se$ (200 μg mL^{-1}) upon MMP-2 pretreatment for 0, 24, and 48 h. c) MB degradation of Fe_3O_4 (200 μg mL^{-1}), $Cu_{1.77}Se$ (165 μg mL^{-1}), and Fe_3O_4@$Cu_{1.77}Se$ (200 μg mL^{-1}) with or without MMP-2 pretreatment for 48 h. d) MB degradation of MMP-2 pretreated Fe_3O_4@$Cu_{1.77}Se$ with or without photoirradiation (1064 nm, 0.75 W cm^{-2}) for 10 min. e) GSH depletion of Fe_3O_4@$Cu_{1.77}Se$ (200 μg mL^{-1}) with or without MMP-2 pretreatment for 0, 24, and 48 h. f) GSH depletion of Fe_3O_4 (200 μg mL^{-1}), $Cu_{1.77}Se$ (165 μg mL^{-1}), and Fe_3O_4@$Cu_{1.77}Se$ (200 μg mL^{-1}) with or without MMP-2 pretreatment. g) GSH depletion of MMP-2 pretreated Fe_3O_4@$Cu_{1.77}Se$ with or without photoirradiation (1064 nm, 0.75 W cm^{-2}). h) TEM images of Fe_3O_4@$Cu_{1.77}Se$ with or without MMP-2 pretreatment for 0, 24, and 48 h. i) T_2-weighted MR and j) PA imaging of Fe_3O_4@$Cu_{1.77}Se$ with or without MMP-2 pretreatment for 48 h.

4.55×10^{-8} M s^{-1} respectively, indicating stronger catalytic ability of Fe_3O_4@$Cu_{1.77}Se$ after MMP-2 treatment (Figure S15, Supporting Information).

Consistently, GSH depletion abilities of Fe_3O_4@$Cu_{1.77}Se$ was also in MMP-2 activatable, photothermal-enhanced manner. Specifically, the characteristic peak of DTNB at 420 nm

decreased fastest in Fe_3O_4@$Cu_{1.77}Se$ treated with MMP-2 for 48 h at all the time points. At 10 min, GSH depletion in Fe_3O_4@$Cu_{1.77}Se$ treated with MMP-2 was increased by 1.4- and 2.3-fold compared to Fe_3O_4 and $Cu_{1.77}Se$, respectively (Figure 2f). Combination with photoirradiation at 1064 nm further decreased the DTNB absorbance to 31.2%, 1.2-fold lower than that without photoirradiation (Figure 2g).

Considering that gelatin, the template for the assembly of Fe_3O_4@$Cu_{1.77}Se$, could be degraded by matrix metalloproteinases, such as MMP-2 or MMP-9, Fe_3O_4@$Cu_{1.77}Se$ in the presence or the absence MMP-2 treatments was collected for both TEM and DLS analysis. In the presence of MMP-2, Fe_3O_4@$Cu_{1.77}Se$ disintegrated gradually with decreased size from 124.2 ± 3.0 to 14.6 ± 6.9 nm over time till 48 h (Figure 2h; Figure S16, Supporting Information). In contrast, in the absence of MMP-2, the size and morphology of Fe_3O_4@$Cu_{1.77}Se$ remained unchanged. These data suggested that MMP-2 triggered the disassembly of Fe_3O_4@$Cu_{1.77}Se$ to generate higher concentrations of reactive iron pools in solution, leading to increased •OH generation and GSH depletion.

Prior to assessing the in vitro therapeutic efficacy of Fe_3O_4@$Cu_{1.77}Se$ towards 4T1 cells, the cellular uptake and intracellular localization of Fe_3O_4@$Cu_{1.77}Se$ were examined (Figures S17 and S18, Supporting Information). Fe_3O_4@$Cu_{1.77}Se$ was conjugated with Cy5, and the fluorescence of Cy5, LysoTracker Green, and Hoechst were utilized to indicate the Fe_3O_4@$Cu_{1.77}Se$, lysosome, and nuclei, respectively. Increased cellular uptake of Fe_3O_4@$Cu_{1.77}Se$ was observed with increasing incubation time and reached the maximum at 6 h. Moreover, the red fluorescence of Cy5 overlapped well with the green fluorescence from LysoTracker Green, suggesting the localization of Fe_3O_4@$Cu_{1.77}Se$ in the lysosomes.

Afterward, in vitro therapeutic efficacy of Fe_3O_4@$Cu_{1.77}Se$ was assessed. In the absence of H_2O_2, Fe_3O_4@$Cu_{1.77}Se$ had negligible toxicity to 4T1 cells even with a concentration up to 100 mg mL^{-1}, indicating its good biocompatibility (Figure S19, Supporting Information). However, in the presence of H_2O_2 (5 mM), the viability decreased to 48.4% in Fe_3O_4@$Cu_{1.77}Se$-treated cells, which was 2.3- and 1.5-fold higher than that in Fe_3O_4- and $Cu_{1.77}Se$-treated groups, respectively. Upon treated with MMP-2, cell viabilities were further decreased to 37.5% and 63.2% in the Fe_3O_4@$Cu_{1.77}Se$- and Fe_3O_4-treated groups, respectively, indicating the enhanced cytotoxicity from the disassembly of Fe_3O_4 and Fe_3O_4@$Cu_{1.77}Se$ in the presence of MMP-2 (**Figure 3**a). With combinational photoirradiation at 1064 nm for 3 min, the cell viability further decreased to 19.9%, which was 1.8- and 1.2-fold lower than those in Fe_3O_4- and $Cu_{1.77}Se$-treated cells, respectively, at the same condition.

Such excellent in vitro therapeutic efficacy can be ascribed to the synergistic enhanced •OH production and GSH-depletion of Fe_3O_4@$Cu_{1.77}Se$ upon combinational treatments with MMP-2 and NIR-II photoirradiation, as evident in Figures 3b,c,e. Significant green fluorescence of DCFH-DA (2',7'-dichlorofluorescein diacetate, a fluorescent turn-on indicator for ROS) was only observed in Fe_3O_4@$Cu_{1.77}Se$-treated cells with MMP-2, while it was weak in both Fe_3O_4- and $Cu_{1.77}Se$-treated cells in the presence or absence of MMP-2. With combinational NIR-II photoirradiation, Fe_3O_4@$Cu_{1.77}Se$-treated cells showed a higher fluorescence compared with that in the absence of photoirradiation, indicating that photothermal treatment significantly facilitated the generation of •OH from Fe_3O_4@$Cu_{1.77}Se$. Meanwhile, DTNB assay indicated that Fe_3O_4@$Cu_{1.77}Se$+MMP-2+photoirradiation-treated cells reduced GSH content to 20.9%, the most significant, while Fe_3O_4@$Cu_{1.77}Se$- and Fe_3O_4@$Cu_{1.77}Se$+MMP-2-treated groups depleted GSH to 50.2% and 35.2%, respectively (Figure 3c). Fe_3O_4- or $Cu_{1.77}Se$-treated cells, regardless of treatments with MMP-2 or photoirradiation, exhibited much weaker GSH depletion capabilities than that in Fe_3O_4@$Cu_{1.77}Se$-treated cells, at the same conditions.

It has been reported that overproduction of •OH and depletion of GSH to inactivate the glutathione peroxidase 4 (GPX4) can lead to the excess accumulation of lipid peroxidation (LPO) inside cells, which is a critical biomarker of ferroptosis.[18] Therefore, the intracellular expression of LPO in 4T1 cells after treatments was then evaluated using BODIPY$^{665/676}$-C11 (a LPO sensor) by confocal laser scanning microscopy (CLSM) (Figure 3d,f). Highest fluorescence was observed in Fe_3O_4@$Cu_{1.77}Se$-treated cells than that in Fe_3O_4- and $Cu_{1.77}Se$-treated cells, suggesting the greatest LPO generation. The signal was further enhanced from 29.75% to 34.9% when Fe_3O_4@$Cu_{1.77}Se$-treated cells were incubated with MMP-2. Combinational photoirradiation at 1064 nm for 4 min further boosted the fluorescence to 44.6%, which was 1.6- and 1.3-fold higher than those in Fe_3O_4- and $Cu_{1.77}Se$-treated cells, respectively, at the same condition.

To further verify the ferroptosis-inducing capability of Fe_3O_4@$Cu_{1.77}Se$, western blot was performed to examine the expression of ferroptosis-related biomarkers, including ferritin, ferroportin-1 (FPN-1), long-chain-fatty-acid-CoA ligase 4 (ACSL4), and GPX4 (Figure 3h). Ferritin is the major intracellular iron storage protein.[19] FPN-1 is the sole iron exporter, of which the downregulation has been indicated to increase intracellular iron retention.[20] ACSL4 is an isozyme that is responsible for the esterification of CoA to free fatty acids and the formation of acyl-CoA activates the corresponding fatty acids for LPO.[21] High ACSL4 expression renders cells more sensitive to ferroptosis by preferentially catalyzing arachidonic acid (AA), and shaping cellular lipid composition. As shown in Figure 3h, the most significantly downregulated expressions of ferritin, FPN-1, ACSL4, and GPX4 were all observed in Fe_3O_4@$Cu_{1.77}Se$+MMP-2+photolirradiation-treated cells, compared with those in groups of PBS, Fe_3O_4@$Cu_{1.77}Se$+MMP-2, Fe_3O_4@$Cu_{1.77}Se$+photoirradiation. Meanwhile, the highest expression of caspase-3 (cas-3), the key enzyme in cell apoptosis, was also observed in Fe_3O_4@$Cu_{1.77}Se$+MMP-2+photoirradiation-treated cells, compared with that in groups of Fe_3O_4@$Cu_{1.77}Se$+MMP-2 and Fe_3O_4@$Cu_{1.77}Se$+photoirradiation, suggesting the occurrence of cas-3 dependent apoptosis. This implies that the degradation of ferritin and FPN-1 by Fe_3O_4@$Cu_{1.77}Se$ upon combinational MMP-2 and photoirradiation treatments synergistically generated more reactive iron pools within cells to induce the imbalanced oxidative stress for enhanced ferroptosis/apoptosis against cancer cells.

The ferroptotic/apoptotic cancer cells induced by Fe_3O_4@$Cu_{1.77}Se$ upon combinational MMP-2 and photoirradiation treatments also elicited the immune response by generation of damage-associated molecular patterns (DAMPs), including calreticulin (CRT), adenosine triphosphate (ATP),

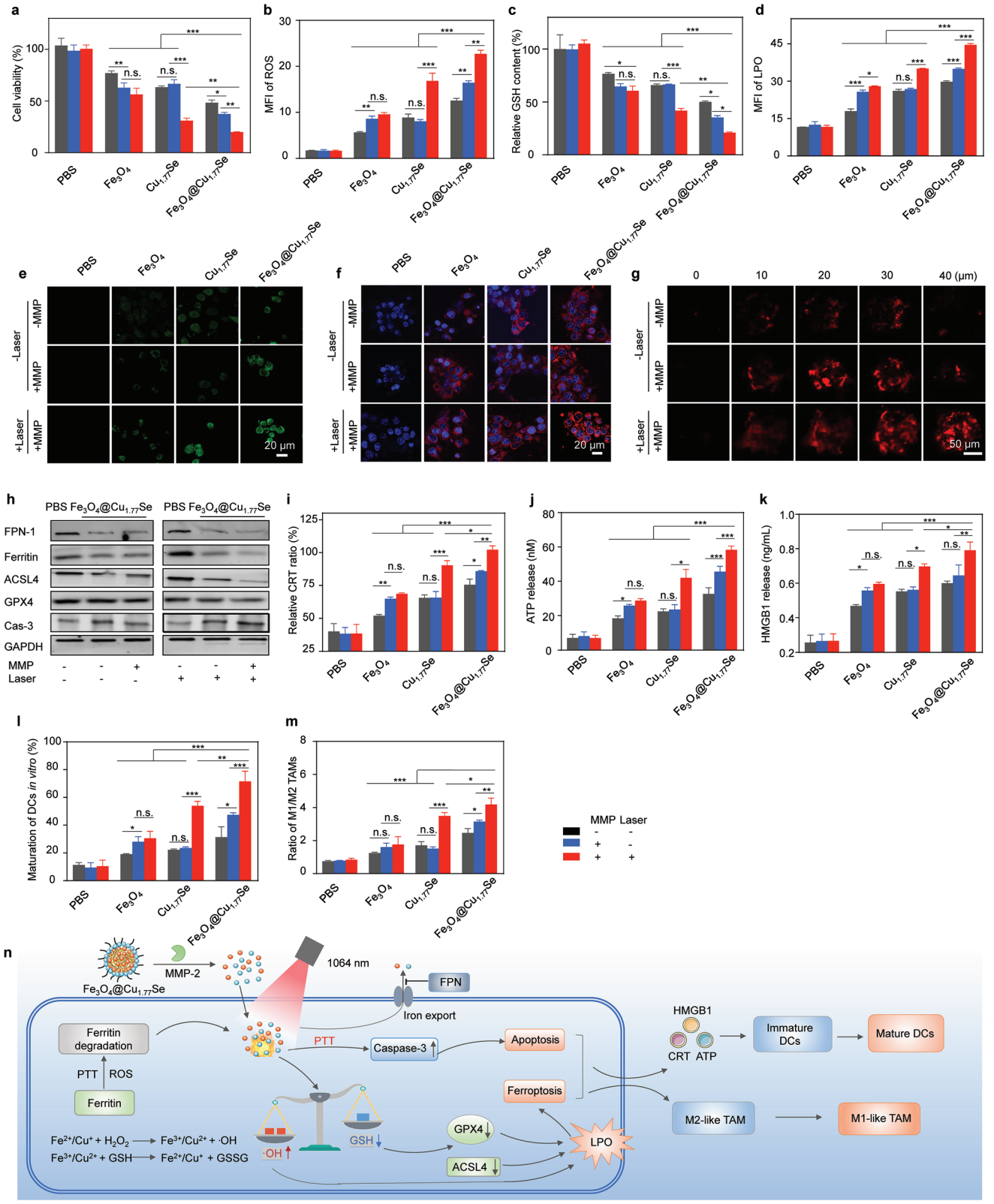

Figure 3. In vitro photothermal ferroptosis anti-tumor therapeutic efficacy evaluation of $Fe_3O_4@Cu_{1.77}Se$ upon treatments. a) Cell viability of 4T1 cells incubated with Fe_3O_4, $Cu_{1.77}Se$, and $Fe_3O_4@Cu_{1.77}Se$ at the concentration of 50 μg mL^{-1} with or without MMP, with MMP and photoirradiation for 3 min (1064 nm, 0.75 W cm^{-2}) in the presence of H_2O_2. b) Fluorescence quantification of ROS in 4T1 cells after incubating with Fe_3O_4, $Cu_{1.77}Se$, and $Fe_3O_4@Cu_{1.77}Se$ at concentration of 50 μg mL^{-1} with or without MMP, with MMP and photoirradiation for 3 min (1064 nm, 0.75 W cm^{-2}). c) Relative GSH content in 4T1 cells incubated with Fe_3O_4, $Cu_{1.77}Se$, and $Fe_3O_4@Cu_{1.77}Se$ at concentration of 50 μg mL^{-1} with or without MMP, with MMP and

and high mobility group box 1 (HMGB1), as evident in Figures 3i–k. Elevated level of CRT in the Fe_3O_4@$Cu_{1.77}$Se-treated cells (75.4%) was observed, as compared to that in Fe_3O_4 (51.9%) and $Cu_{1.77}$Se (65.54%)-treated cells. With MMP-2 treatment, the signals were enhanced to 85.9% and 64.8% in Fe_3O_4@$Cu_{1.77}$Se and Fe_3O_4-treated cells, respectively, whereas similar CRT level was observed in $Cu_{1.77}$Se-treated cells (Figure S20, Supporting Information). Combinational photoirradiation at 1064 nm for 3 min boosted the CRT content in Fe_3O_4@$Cu_{1.77}$Se-treated cells, which was 1.5- and 1.1-fold higher than those in Fe_3O_4 and $Cu_{1.77}$Se-treated cells, respectively, at the same condition. Similar trends were also observed for the release of ATP and HMGB1 in Fe_3O_4@$Cu_{1.77}$Se+MMP-2+photoirradiation-treated cells (Figure 3j,k). These results verified that Fe_3O_4@$Cu_{1.77}$Se by combinational MMP-2 and photoirradiation treatments triggered efficient generation of immunogenic cell death (ICD).

Since the translocation of CRT in endoplasmic reticulum to cell surface, release of ATP, and exposure of HMGB1 on the surface of apoptotic cells can facilitate the uptake, processing, and presentation of tumor antigens by dendritic cells (DCs), the capability of Fe_3O_4@$Cu_{1.77}$Se to promote DCs maturation was next assessed.[22] The matured ratio of DCs ($CD80^+CD86^+$) for Fe_3O_4@$Cu_{1.77}$Se+MMP-2+photoirradiation was 71.6%, which was 2.3- and 1.5-fold higher than that in groups of Fe_3O_4@$Cu_{1.77}$Se and Fe_3O_4@$Cu_{1.77}$Se+MMP-2, respectively (Figure S21, Supporting Information). By contrast, Fe_3O_4- and $Cu_{1.77}$Se-treated groups showed obviously decreased DCs maturation ratio. Noted that with photoirradiation, nearly one-fold enhanced maturation ratio of DCs by $Cu_{1.77}$Se was observed, indicating that photothermal treatment elevated the levels of ICD to facilitate the DCs maturation. Along with DCs maturation, the polarization of M2-like macrophages to M1 phenotype by Fe_3O_4@$Cu_{1.77}$Se was evaluated in IL-4-conditioned RAW 264.7 cells (Figure 3m; Figure S22, Supporting Information). Compared with PBS, Fe_3O_4, and $Cu_{1.77}$Se, Fe_3O_4@$Cu_{1.77}$Se exhibited significantly enhanced expression of $CD80^+$ and $CD86^+$ (M1-related markers), while decreased expression of $CD206^+$ (M2-related marker), suggesting the excellent M2 macrophage repolarization activity of Fe_3O_4@$Cu_{1.77}$Se. Together, these results verified that Fe_3O_4@$Cu_{1.77}$Se by MMP-2 and photoirradiation not only triggered efficient generation of ICD to induce the maturation of DCs, but also reprogramed M2 phenotype to M1 macrophages in vitro. The molecular ferroptosis-based therapeutic mechanism and immune stimulation of Fe_3O_4@$Cu_{1.77}$Se-mediated cancer therapy in vitro were summarized in Figure 3n.

Of note, the disassembled Fe_3O_4@$Cu_{1.77}$Se upon MMP-2 and photoirradiation treatment exhibited deeper penetration depth in 4T1 multicellular spheroids (MCS), at each tested depth, compared to those without treatment and MMP-2 only (Figure 3g). At the depth of 30 μm, the mean fluorescence intensity of Fe_3O_4@$Cu_{1.77}$Se after photoirradiation was 4.5- and 2.2-fold higher than that without treatments and MMP-2 only (Figure S23, Supporting Information).

After verifying the excellent therapeutic performance in vitro, the feasibility of Fe_3O_4@$Cu_{1.77}$Se for cancer theranostics in vivo was examined. First, the potential of Fe_3O_4@$Cu_{1.77}$Se as MMP-2 activatable MRI contrast agents in vivo was evaluated by intratumoral (i.t) injection. The tumor models were established by subcutaneous injection of 4T1 cells into both flanks of each mouse, followed by intratumoral injection of Fe_3O_4@$Cu_{1.77}$Se into the right tumor site of the mice. Afterward, both sides were imaged at different time points. Enhanced MRI signals overtime were only observed in the right tumor site of mice treated with Fe_3O_4@$Cu_{1.77}$Se, whereas signal changes were negligible in the nontreated left tumor tissues, validating the MMP-2 activatable MRI contrast enhancement ability of Fe_3O_4@$Cu_{1.77}$Se for tumor-specific imaging and theranostics (**Figures 4**a,b).

Subsequently, in vivo therapeutic performance of Fe_3O_4@$Cu_{1.77}$Se was evaluated. 4T1 tumor-bearing BALB/c mice models were established by subcutaneous injection of 4T1 cells into both flanks of each mouse as the primary and distant tumors. After the primary tumor volume reached 100 mm^3, mice were intravenously injected with PBS, Fe_3O_4, $Cu_{1.77}$Se, and Fe_3O_4@$Cu_{1.77}$Se, followed by local NIR-II photoirradiation (Figure 4c). The growths of both primary and distant tumors and lung metastasis were monitored after treatments. To verify the optimal time-point for photoirradiation, MR and PA imaging were conducted on the 4T1 tumor-bearing mice. Noted that an external magnetic field was applied to the primary tumor of mice to enhance the accumulation of nanoparticles. Both MRI and PA signals in tumor tissues after Fe_3O_4@$Cu_{1.77}$Se injection gradually increased over time and reached the plateau at 12 h post-injection time (Figures 4d–g). Therefore, therapeutic treatment was conducted by photoirradiation of the primary tumor with 1064 nm laser at 12 h post-injection of Fe_3O_4@$Cu_{1.77}$Se. The tumors of Fe_3O_4@$Cu_{1.77}$Se-injected mice exhibited the highest temperature increase, followed by $Cu_{1.77}$Se and Fe_3O_4 after 10 min photoirradiation, which can be attributed to the higher accumulation of Fe_3O_4@$Cu_{1.77}$Se in the tumor due to the external magnetic field (Figure 4h; Figure S24, Supporting Information). After photoirradiation, the primary tumors in Fe_3O_4@$Cu_{1.77}$Se-injected mice were almost inhibited, while the growth of primary tumors in Fe_3O_4 and $Cu_{1.77}$Se was inhibited by 1.5- and 1.3-fold compared to those in the control mice

photoirradiation for 3 min (1064 nm, 0.75 W cm^{-2}). d) Quantification of LPO in 4T1 cells incubated with Fe_3O_4, $Cu_{1.77}$Se, and Fe_3O_4@$Cu_{1.77}$Se at concentration of 50 μg mL^{-1} with or without MMP, with MMP and photoirradiation for 3 min (1064 nm, 0.75 W cm^{-2}). e) Confocal fluorescence images of ROS production and f) LPO content in 4T1 cells after incubating with Fe_3O_4, $Cu_{1.77}$Se, and Fe_3O_4@$Cu_{1.77}$Se at concentration of 50 μg mL^{-1} with or without MMP, with MMP and photoirradiation for 3 min (1064 nm, 0.75 W cm^{-2}). ROS were indicated by DCFH-DA (green fluorescence), LPO was stained with the red-fluorescent probe BODIPY 665/676, and nuclei were stained with DAPI. g) Confocal fluorescence images of 4T1 MCSs incubated with Fe_3O_4, $Cu_{1.77}$Se, and Fe_3O_4@$Cu_{1.77}$Se at concentration of 50 μg mL^{-1} with or without MMP, with MMP and photoirradiation for 3 min (1064 nm, 0.75 W cm^{-2}). h) Western blots analysis of expression of ferroptosis and apoptosis-related proteins in 4T1 cells after incubated with Fe_3O_4, $Cu_{1.77}$Se, and Fe_3O_4@$Cu_{1.77}$Se at concentration of 50 μg mL^{-1} with or without MMP, with MMP and photoirradiation for 3 min (1064 nm, 0.75 W cm^{-2}). i) Flow cytometry quantification of CRT on the surface of 4T1 breast tumor cells. j) ATP secretion from 4T1 breast tumor cells was measured by ATP assay kit. k) HMGB1 released by 4T1 breast tumor cells was quantified via ELISA kit. l) Flow cytometry quantification of DCs maturation after incubating with Fe_3O_4, $Cu_{1.77}$Se, and Fe_3O_4@$Cu_{1.77}$Se at concentration of 50 μg mL^{-1} with or without MMP, with MMP and photoirradiation for 3 min (1064 nm, 0.75 W cm^{-2}). m) Flow cytometry quantification of ratio of M1/M2 TAMs. $*p < 0.05$, $**p < 0.01$, and $***p < 0.001$.

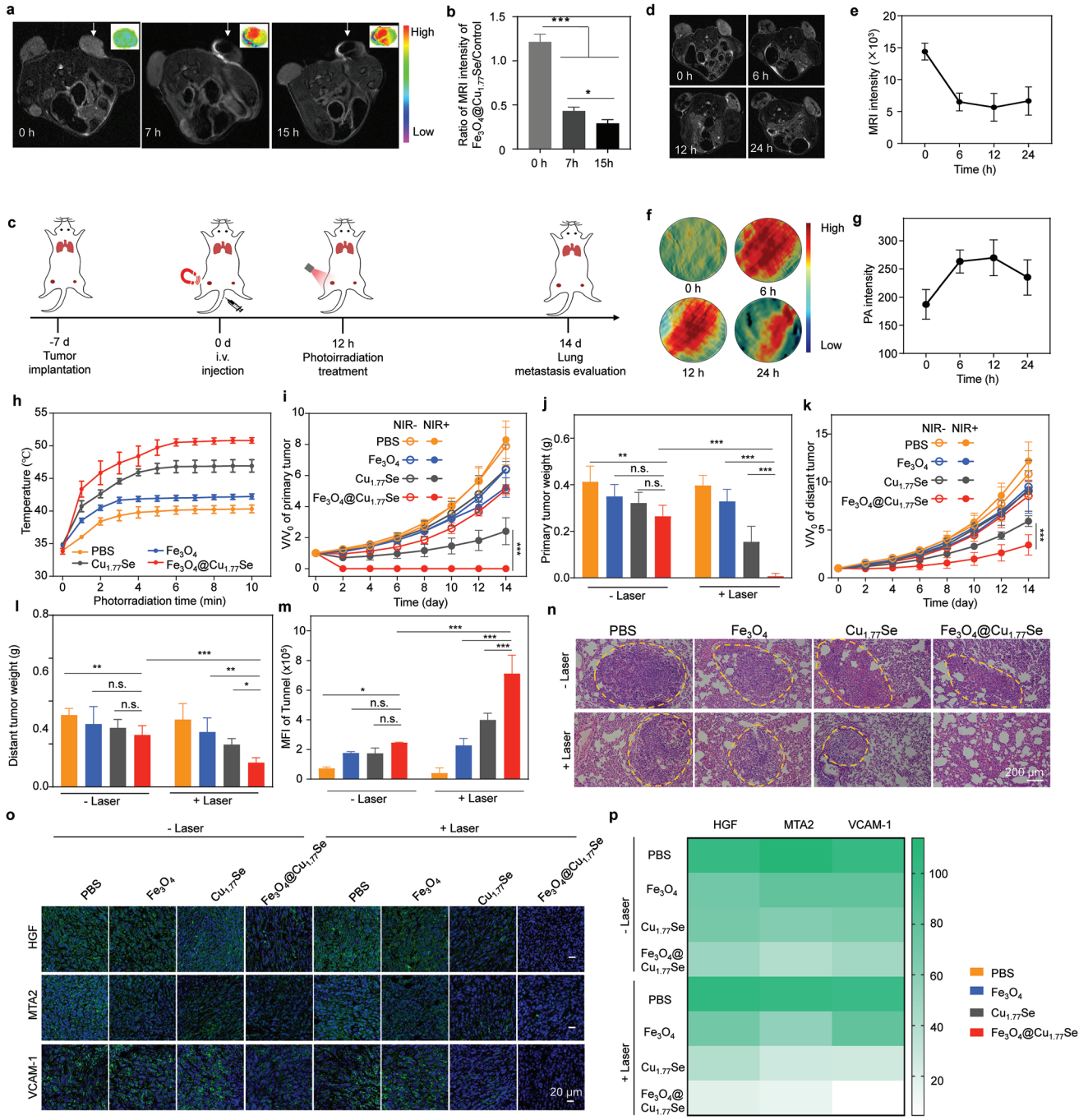

Figure 4. In vivo imaging-guided therapeutic evaluation of Fe_3O_4@$Cu_{1.77}Se$ upon treatments. a) MR imaging and b) the ratio of MRI signal intensity of Fe_3O_4@$Cu_{1.77}Se$ vs PBS after i.t. injection. The left tumors were injected with PBS and the right tumors were injected with Fe_3O_4@$Cu_{1.77}Se$ (2 mg mL^{-1}, 20 μL). c) Schedule of tumor implantation and therapeutic evaluation of Fe_3O_4@$Cu_{1.77}Se$ upon treatments. d) MR imaging and e) quantification of 4T1 tumors after i.v. injection of Fe_3O_4@$Cu_{1.77}Se$ with magnet treatment. f) PA imaging and g) quantification of 4T1 tumors after i.v. injection of Fe_3O_4@$Cu_{1.77}Se$. h) Temperature increase of 4T1 tumors upon 1064 nm photoirradiation (0.75 W cm^{-2}, 10 min) at 12 h after i.v. injection of PBS, Fe_3O_4, $Cu_{1.77}Se$, and Fe_3O_4@$Cu_{1.77}Se$, respectively. Tumor growth curves of i) primary and k) distant 4T1 tumors after treatments. Weight of j) primary and l) distant 4T1 tumors from scarificed mice after treatments on day 14. m) Quantification of Tunnel imaging in 4T1 tumors after treatments. n) H&E staining of lungs after treatments. o) Immunofluorescence images and p) quantification of metastasis-related proteins including HGF, MTA2, and VCAM-1, in 4T1 tumor tissues after treatments. Cell nuclei were stained by DAPI with blue fluorescence. HGF, MTA2, and VCAM-1 were stained by respective antibodies with green fluorescence. *$p < 0.05$, **$p < 0.01$, and ***$p < 0.001$.

(Figures 4i,j; Figure S25, Supporting Information). In distant tumors, the inhibition rate in Fe_3O_4@$Cu_{1.77}$Se-injected mice with photoirradiation was 3.9-, 3.0-, and 1.8-fold lower compared to PBS, Fe_3O_4 and $Cu_{1.77}$Se, respectively (Figures 4k,l).

Moreover, fewer metastatic nodules were observed in the lungs of Fe_3O_4@$Cu_{1.77}$Se-injected mice with photoirradiation, while obvious pulmonary tumor metastases were observed for mice in other treatment groups (Figure 4p; Figures S26, S27, Supporting Information). Quantitative analysis showed that the number of metastatic nodules in the lungs of Fe_3O_4@$Cu_{1.77}$Se-injected mice with photoirradiation was 3.2-, 2.7-, and 1.5-fold lower than those in the Fe_3O_4@$Cu_{1.77}$Se-injected mice without photoirradiation, Fe_3O_4-, and $Cu_{1.77}$Se-injected mice with photoirradiation, respectively. Of note, no visible nucleus and cytoplasm alterations or abnormalities in major organs, including heart, liver, spleen, and kidney from mice were observed in the histological examination by hematoxylin and eosin (H&E) stain on day 14 (Figure S28, Supporting Information). No weight loss in the mice was noticed by monitoring the body weight for 14 days after treatment (Figure S29, Supporting Information).

To understand how Fe_3O_4@$Cu_{1.77}$Se inhibited the metastasis, the expressions of metastasis-related proteins including hepatocyte growth factor (HGF), metastasis-associated protein 2 (MTA2), and vascular cell adhesion molecule-1 (VCAM-1) in tumor tissues after treatments were investigated by immunofluorescence staining (Figures 4o,p). Weak green fluorescence of HGF, MTA2, and VCAM-1 staining was observed in Fe_3O_4@$Cu_{1.77}$Se-injected tumors with photoirradiation, indicating low expressions of these metastasis-related proteins. By contrast, intense green fluorescence signals were observed in the tumors for other treatment groups. Quantitative studies indicated that the expressions of HGF, MTA2, and VCAM-1 were reduced to 17.8%, 9.7%, and 4.5% in Fe_3O_4@$Cu_{1.77}$Se-injected tumors with photoirradiation, respectively, compared with 67.6%, 60.2%, and 76.3% in Fe_3O_4, 65.6%, 58.7%, and 71.5% in $Cu_{1.77}$Se and 96.8%, 96.8%, and 95.0% in PBS-injected tumors, respectively. Collectively, these data suggested the synergistic antitumor effect of Fe_3O_4@$Cu_{1.77}$Se for cancer therapy.

To gain more insight into the in vivo synergistic therapeutic mechanism of Fe_3O_4@$Cu_{1.77}$Se, generation of ROS, and expression of ferroptosis/apoptosis proteins, including GPX4, ACSL-4, LPO as well as caspase-3, in tumor tissues after 24 h post-injection of PBS, Fe_3O_4, $Cu_{1.77}$Se, and Fe_3O_4@$Cu_{1.77}$Se were collected for further immunofluorescence staining (**Figures 5**a–f). Overall, Fe_3O_4@$Cu_{1.77}$Se-injected tumors with photoirradiation displayed the highest ROS generation and ferroptosis/apoptosis-inducing capabilities than those in other treatments. For instance, with 10 min photoirradiation, the fluorescence of DCFH-DA in Fe_3O_4@$Cu_{1.77}$Se-injected tumors was enhanced from 55.4% to 99.1%, compared to that in PBS (from 7.2% to 7.5%), Fe_3O_4 (from 24.8% to 42.2%), and $Cu_{1.77}$Se (from 39.0% to 74.2%)-injected tumors. The expressions of GPX-4 and ACSL4 in Fe_3O_4@$Cu_{1.77}$Se-treated tumor with photoirradiation were decreased from 53.9% to 11.5%, and 42.5% to 10.2%, respectively, which subsequently induced significantly stronger fluorescence of LPO. Similarly, caspase-3 expression in Fe_3O_4@$Cu_{1.77}$Se-treated tumors with photoirradiation was 93.9%, in contrast to those cells treated with PBS (6.3%), Fe_3O_4 (26.9%), or $Cu_{1.77}$Se (28.1%), respectively.

Subsequently, the generation of HMGB1 and CRT, maturation of DCs in lymph nodes, and activation of immune response in vivo were investigated. HMGB1 in the Fe_3O_4@$Cu_{1.77}$Se-injected tumors with photoirradiation was increased by 9.1-, 2.6-, and 1.4-fold compared to PBS, Fe_3O_4, and $Cu_{1.77}$Se group, respectively, at the same condition (Figure 5g). Similarly, the level of CRT in the Fe_3O_4@$Cu_{1.77}$Se-injected tumor with photoirradiation was 11.4-,2.8-, and 1.4-fold compared to that in PBS-, Fe_3O_4-, and $Cu_{1.77}$Se-injected groups, respectively (Figure 5h). The efficient generation of ICD triggered by Fe_3O_4@$Cu_{1.77}$Se in vivo promotes the maturation of DCs, activation of $CD8^+$ T cells, and polarization of tumor-associated macrophage. Specifically, with photoirradiation, the populations of matured DCs for Fe_3O_4@$Cu_{1.77}$Se groups increased by 1.4-, 1.3-, and 1.7-fold compared to Fe_3O_4, $Cu_{1.77}$Se and control groups, respectively (Figure 5i; Figure S30, Supporting Information). Meanwhile, the highest population of $CD8^+$ T cells was also observed in Fe_3O_4@$Cu_{1.77}$Se-treated tumors with photoirradiation, which was 1.9-, 2.0-, and 2.4-fold higher than those for Fe_3O_4, $Cu_{1.77}$Se and PBS groups, respectively (Figure 5j; Figure S31, Supporting Information). The polarization of M2 to M1 in Fe_3O_4@$Cu_{1.77}$Se-treated tumor with photoirradiation increased by 2.2, 1.5-, and 2.7-fold compared to Fe_3O_4, $Cu_{1.77}$Se and control groups, respectively (Figure 5l). By contrast, no noticeable changes in the populations of matured DCs, infiltrative $CD8^+$ T cells, and polarization of M2 to M1, were observed for other treatment groups. With photoirradiation, the serum levels of IFN-γ were increased by 1.6- and 1.4-fold in Fe_3O_4@$Cu_{1.77}$Se-injected tumors as compared to Fe_3O_4- and $Cu_{1.77}$Se-injected tumors, respectively. Similarly, with photoirradiation, TNF-α was increased by 1.4-, and 1.2-fold in Fe_3O_4@$Cu_{1.77}$Se-injected tumors as compared to that in Fe_3O_4- and $Cu_{1.77}$Se-injected tumors, respectively (Figures 5k,m). The immune stimulation of Fe_3O_4@$Cu_{1.77}$Se-mediated photothermal ferroptosis cancer therapy in vivo was summarized in Figure 5n. Together, these results provided strong evidence that the Fe_3O_4@$Cu_{1.77}$Se-mediated ferroptosis-based second NIR photothermal therapy not only generated strong ICD to induce maturation of DCs that facilitated the activation and infiltration of cytotoxic $CD8^+$ T cells into the immunogenetic cold tumor (4T1), but also polarized M2 tumor-associated macrophages to M1 tumor-associated macrophages, thereby leading to the effective inhibition of primary and distant tumors as well as lung metastasis.

3. Conclusions

In summary, we have developed a novel MMP-2 activatable, second NIR photothermal-enhanced theranostic nanozyme based on Fe_3O_4@$Cu_{1.77}$Se for high-performance cancer therapy. The overexpressed MMP-2 in tumor microenvironment disassembles Fe_3O_4@$Cu_{1.77}$Se to enhance reactive intratumor ferrous supply for elevated ferrotherapeutic effect and enhanced T_2-weighted MRI contrast. Combinational NIR-II photoirradiation not only triggers effective photothermal therapy, but more importantly, significantly potentiates Fenton reaction to generate substantial hydroxyl radicals and consume GSH to induce more lipid peroxidation for boosted ferroptosis. Such synergism induces immunogenic cell death to enhance the

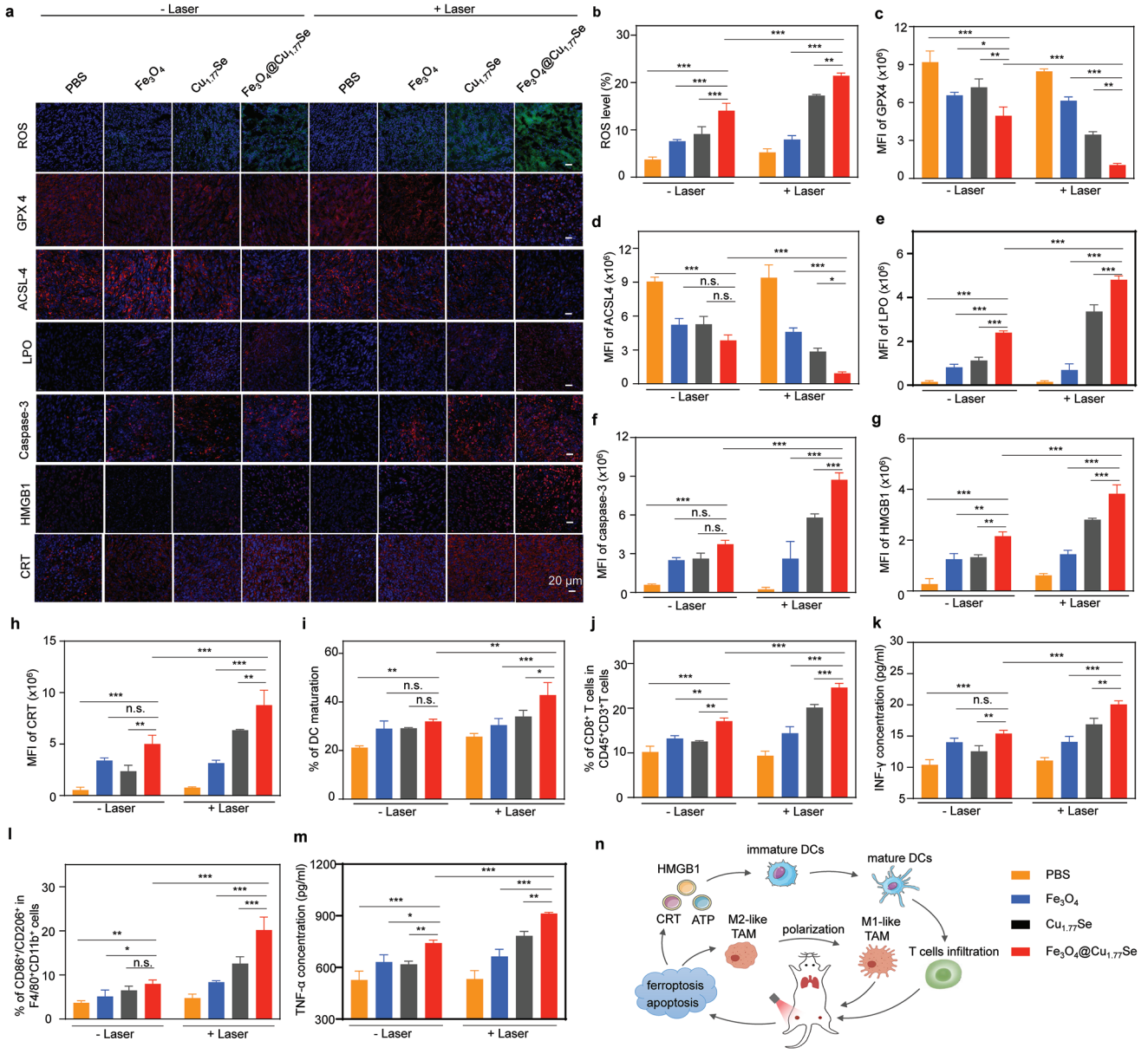

Figure 5. In vivo therapeutic mechanism of Fe_3O_4@$Cu_{1.77}Se$ for photothermal ferroptosis cancer therapy. a) Immunofluorescence images and b–h) quantification of ROS, LPO, GPX-4, ACSL-4, caspase-3, HMGB1, and CRT in 4T1 tumors after treatments. ROS was indicated with green color. LPO, GPX-4, ACSL-4, caspase-3, HMGB1, and CRT were indicated with red color. Cell nuclei were stained by DAPI with blue color. i) Quantification of DCs maturation in lymph nodes on day 3 after treatments ($n = 3$). j) Quantification of the ratio of $CD8^+$ T cells in $CD45^+CD3^+$ T cells of 4T1 tumors on day 5 after treatments ($n = 3$). k) Quantitative analysis of IFN-γ in the serum of 4T1 tumor-bearing mice after different treatments on day 14 ($n = 3$). l) Ratio of M_1/M_2-like TAM in 4T1 tumors on day 5 after treatments ($n = 3$). m) TNF-α secretion in the serum of 4T1 tumor-bearing mice after treatments on day 14 ($n = 3$). n) Mechanistic scheme of Fe_3O_4@$Cu_{1.77}Se$-induced anticancer effect in vivo. *$p < 0.05$, **$p < 0.01$, and ***$p < 0.001$.

cytotoxic T cells recruitment and infiltration into the immunogenetic cold tumor, and also, polarizes M2 tumor-associated macrophages to M1 tumor-associated macrophages. As such, it can efficiently eliminate the primary tumors, and elicits systemic anti-tumor immunity, contributing to regression of non-treated distant tumors and inhibition of lung metastasis. Thus, this study provides a promising activatable nanozyme design strategy for photothermal ferroptosis cancer therapy with high spatial-temporal specificity.

Supporting Information

Supporting Information is available from the Wiley Online Library or from the author.

Acknowledgements

W.Q. and J.H. contributed equally to this work. The authors thank National Key R&D Program of China (2021YFA1201200) for financial

support. The authors also thank the Analytical and Testing Centre of Huazhong University of Science and Technology for related analysis. All animal experiments were carried out as per the guidelines and upon approval of the Institutional Animal Care and Use Commitee of Huazhong University of Science and Technology, China.

Conflict of Interest

The authors declare no conflict of interest.

Data Availability Statement

The data that support the findings of this study are available in the supplementary material of this article.

Keywords

photoacoustic imaging, photothermal ferroptosis cancer therapy, protease-activatable nanozymes, tumor-enhanced magnetic resonance imaging

Received: August 23, 2022
Revised: September 29, 2022
Published online: November 18, 2022

[1] S. J. Dixon, K. M. Lemberg, M. R. Lamprecht, R. Skouta, E. M. Zaitsev, C. E. Gleason, D. N. Patel, A. J. Bauer, A. M. Cantley, W. S. Yang, B. Morrison3rd, B. R. Stockwell, *Cell* **2012**, *149*, 1060.
[2] V. Trujillo-Alonso, E. C. Pratt, H. Zong, A. Lara-Martinez, C. Kaittanis, M. O. Rabie, V. Longo, M. W. Becker, G. J. Roboz, J. Grimm, M. L. Guzman, *Nat. Nanotechnol.* **2019**, *14*, 616.
[3] H. Liu, R. Jiang, Y. Lu, B. Shan, Y. Wen, M. Li, *ACS App. Mater. Interfaces* **2022**, *14*, 28537.
[4] S. E. Kim, L. Zhang, K. Ma, M. Riegman, F. Chen, I. Ingold, M. Conrad, M. Z. Turker, M. Gao, X. Jiang, S. Monette, M. Pauliah, M. Gonen, P. Zanzonico, T. Quinn, U. Wiesner, M. S. Bradbury, M. Overholtzer, *Nat. Nanotechnol.* **2016**, *11*, 977.
[5] X. Liu, X. Zhu, X. Qi, X. Meng, K. Xu, *Int. J. Nanomed.* **2021**, *16*, 1037.
[6] C. Zhang, W. Bu, D. Ni, S. Zhang, Q. Li, Z. Yao, J. Zhang, H. Yao, Z. Wang, J. Shi, *Angew. Chem., Int. Ed.* **2016**, *55*, 2101.
[7] a) W. Ni, Y. Li, L. Liang, S. Yang, M. Zhan, C. Lu, L. Lu, L. Wen, *J. Biomed. Nanotechnol.* **2022**, *18*, 327; b) H. Chi, G. Zhu, Y. Yin, H. Diao, Z. Liu, S. Sun, Z. Guo, W. Xu, J. Xu, C. Cui, X.-J. Xing, K. Ma, *Int. J. Pharm.* **2022**, *622*, 121898; c) X. Tan, J. Huang, Y. Wang, S. He, L. Jia, Y. Zhu, K. Pu, Y. Zhang, X. Yang, *Angew. Chem. Int. Ed.* **2021**, *60*, 14051.
[8] a) S. He, Y. Jiang, J. Li, K. Pu, *Angew. Chem. Int. Ed.* **2020**, *59*, 10633; b) C. Xu, K. Pu, *Chem. Soc. Rev.* **2021**, *50*, 1111; c) S. Dong, Y. Dong, T. Jia, S. Liu, J. Liu, D. Yang, F. He, S. Gai, P. Yang, J. Lin, *Adv. Mater.* **2020**, *32*, 2002439.
[9] J. Zhu, P. Dai, F. Liu, Y. Li, Y. Qin, Q. Yang, R. Tian, A. Fan, S. d. F. Medeiros, Z. Wang, Y. Zhao, *Nano Lett.* **2020**, *20*, 6235.
[10] a) Z. Yu, W. K. Chan, Y. Zhang, T. T. Y. Tan, *Biomaterials* **2021**, *269*, 120459; b) A. M. Smith, M. C. Mancini, S. Nie, *Nat. Nanotechnol.* **2009**, *4*, 710; c) J. Huang, J. Li, X. Zhang, W. Zhang, Z. Yu, B. Ling, X. Yang, Y. Zhang, *Nano Lett.* **2020**, *20*, 5236.
[11] J. Jia, G. Liu, W. Xu, X. Tian, S. Li, F. Han, Y. Feng, X. Dong, H. Chen, *Angew. Chem., Int. Ed.* **2020**, *59*, 14443.
[12] B. Tian, S. Liu, L. Feng, S. Liu, S. Gai, Y. Dai, L. Xie, B. Liu, P. Yang, Y. Zhao, *Adv. Funct. Mater.* **2021**, *31*, 2100549.
[13] Z. Xu, N. Rao, C.-Y. Tang, C.-H. Cheng, W.-C. Law, *ACS Omega* **2019**, *4*, 14655.
[14] a) J. Li, X. Yu, Y. Jiang, S. He, Y. Zhang, Y. Luo, K. Pu, *Adv. Mater.* **2021**, *33*, 2003458; b) C. Xu, Y. Jiang, Y. Han, K. Pu, R. Zhang, *Adv. Mater.* **2021**, *33*, 2008061.
[15] Y. Jiang, X. Zhao, J. Huang, J. Li, P. K. Upputuri, H. Sun, X. Han, M. Pramanik, Y. Miao, H. Duan, K. Pu, R. Zhang, *Nat. Commun.* **2020**, *11*, 1857.
[16] M. Chang, Z. Hou, M. Wang, C. Yang, R. Wang, F. Li, D. Liu, T. Peng, C. Li, J. Lin, *Angew. Chem. Int. Ed.* **2021**, *60*, 12971.
[17] C. Ou, W. Na, W. Ge, H. Huang, F. Gao, L. Zhong, Y. Zhao, X. Dong, *Angew. Chem. Int. Ed.* **2021**, *60*, 8157.
[18] W. S. Yang, R. SriRamaratnam, M. E. Welsch, K. Shimada, R. Skouta, V. S. Viswanathan, J. H. Cheah, P. A. Clemons, A. F. Shamji, C. B. Clish, L. M. Brown, A. W. Girotti, V. W. Cornish, S. L. Schreiber, B. R. Stockwell, *Cell* **2014**, *156*, 317.
[19] P. Arosio, L. Elia, M. Poli, *IUBMB Life* **2017**, *69*, 414.
[20] I. Yanatori, D. R. Richardson, K. Imada, F. Kishi, *J. Biol. Chem.* **2016**, *291*, 17303.
[21] S. Doll, B. Proneth, Y. Y. Tyurina, E. Panzilius, S. Kobayashi, I. Ingold, M. Irmler, J. Beckers, M. Aichler, A. Walch, H. Prokisch, D. Trümbach, G. Mao, F. Qu, H. Bayir, J. Füllekrug, C. H. Scheel, W. Wurst, J. A. Schick, V. E. Kagan, J. P. F. Angeli, M. Conrad, *Nat. Chem. Biol.* **2017**, *13*, 91.
[22] a) D. V. Krysko, A. D. Garg, A. Kaczmarek, O. Krysko, P. Agostinis, P. Vandenabeele, *Nat. Rev. Cancer* **2012**, *12*, 860; b) M. Fan, L. Jia, M. Pang, X. Yang, Y. Yang, S. Kamel Elyzayati, Y. Liao, H. Wang, Y. Zhu, Q. Wang, *Adv. Funct. Mater.* **2021**, *31*, 2010587.